Designing Robust Hierarchically Textured Oleophobic Fabrics

Citation: Kleingartner, Justin A.; Srinivasan, Siddarth; Truong, Quoc T.; Sieber, Michael; Cohen, Robert E. and McKinley, Gareth H. "Designing Robust Hierarchically Textured Oleophobic Fabrics." Langmuir 31, no. 48 (December 2015): 13201–13213 © 2015 American Chemical Society

As Published: http://dx.doi.org/10.1021/acs.langmuir.5b03000

Publisher: American Chemical Society (ACS)

Persistent URL: http://hdl.handle.net/1721.1/109349

Version: Author's final manuscript: final author's manuscript post peer review, without publisher's formatting or copy editing

Designing robust hierarchically-textured oleophobic fabrics

Justin A. Kleingartner,[†,§] Siddarth Srinivasan,[†,§] Quoc T. Truong,[‡] Michael Sieber,[‡] Robert E. Cohen,[*,†] and Gareth H. McKinley[*,¶]

†*Department of Chemical Engineering, Massachusetts Institute of Technology, Cambridge, MA 02139*

‡*Research, Development and Engineering Command, US Army Natick Soldier, Research, Development and Engineering Center, Natick, MA 01760*

¶*Department of Mechanical Engineering, Massachusetts Institute of Technology, Cambridge, MA 02139*

§*Contributed equally to this work*

E-mail: recohen@mit.edu; gareth@mit.edu

Abstract

Commercially available woven fabrics (*e.g.*, nylon- or PET-based fabrics) possess inherently re-entrant textures in the form of cylindrical yarns and fibers. We analyze the liquid repellency of woven and nano-textured oleophobic fabrics using a nested model with n levels of hierarchy that is constructed from modular units of cylindrical and spherical building blocks. At each level of hierarchy, the density of the topographical features is captured using a dimensionless textural parameter D_n^*. For a plain-woven mesh comprised of chemically treated fiber bundles ($n = 2$), the tight packing of individual fibers in each bundle ($D_2^* \approx 1$) imposes a geometric constraint on the maximum oleophobicity that can be achieved solely by modifying the surface

energy of the coating. For liquid droplets contacting such tightly bundled fabrics with modified surface energies, we show that this model predicts a lower bound on the equilibrium contact angle of $\theta_E \approx 57^\circ$ below which the Cassie-Baxter to Wenzel wetting transition occurs spontaneously and this is validated experimentally. We demonstrate how the introduction of an additional higher order micro/nano-texture onto the fibers ($n = 3$) is necessary to overcome this limit and create more robustly non-wetting fabrics. Finally, we show a simple experimental realization of the enhanced oleophobicity of fabrics by depositing spherical microbeads of poly(methyl methacrylate)/fluorodecyl polyhedral oligomeric silsesquioxane (fluorodecyl POSS) onto the fibers of a commercial woven nylon fabric.

Introduction

The fabrication of non-wetting surfaces and coatings that repel low surface tension oils and organic liquids in the Cassie-Baxter state requires the presence of re-entrant topographies coupled with low surface energy coatings.[1–3] Commercially available woven fabrics possess inherently re-entrant textures in the form of cylindrical yarns and fibers. Various coating techniques including dip-coating,[4–6] chemical vapor deposition[7–9] and fluorosilane/acrylate chemistry[10–14] have been used to chemically modify the surface energy of woven fabrics and impart an oleophobic character. This allows the treated fabric to support low surface tension drops (*e.g.*, alkanes and organic liquids) in the non-wetting Cassie-Baxter state.[15] However, despite exhibiting large values of the apparent contact angles, these liquid drops are inherently metastable,[3,16] and irreversibly transition to a fully-wetted state if the liquid makes contact with a sufficiently large defect in the re-entrant topography, or a sufficiently large pressure differential is imposed across the composite Cassie-Baxter interface (*e.g.*, an impacting drop, jet, spray, or submersion in a large reservoir of fluid).[17] In order to enhance the robustness of the wetting transition on structured non-wetting surfaces (including woven fabrics), merely designing surfaces

with large values of the macroscopic apparent contact angle is not sufficient. Instead, the relevant oleophobic character of these surfaces is governed by the degree to which they resist transition to a fully-wetted Wenzel state. In this context, designing fabrics that maximize oleophobicity involves understanding how the weave structure and chemical coating concomitantly influence the Cassie-Baxter to Wenzel wetting transition.[15,18] The development of such a framework attains further significance in the context of designing fabrics that are resistant to wetting upon impact by chemical weapons/sprays consisting of low surface tension liquid droplets of small radii with correspondingly large internal Laplace pressures.[19]

Multifilament woven fabrics can be modeled as hierarchically recursive microstructures.[20] They consist of groups of adjacent cylindrical fibers that are wound together to form cylindrically bundled yarns, which are subsequently woven into fabrics.[21] The design principles of hierarchical non-wetting structures were first investigated by Herminghaus,[22] who established a recursive Cassie-Baxter expression for the value of the macroscopically observable contact angle (henceforth denoted θ^*) on hierarchically textured surfaces and emphasized the possibility that for sufficiently high levels of structural recursion any non-zero value of the equilibrium contact angle (denoted θ_E) is sufficient to engineer liquid and oil repellent hierarchical surfaces with large macroscopic contact angles. More recently, Paxson *et al.*[23] investigated the self-similar depinning of the three-phase contact line at the edge of liquid drops sitting on various hierarchically structured non-wetting surfaces, and proposed design principles by which these recursive structures can be engineered to reduce pinning and increase the liquid repellency.

The seminal work of Cassie and Baxter,[24,25] conducted in the 1940s, on understanding the water-repellency of porous substrates was initially formulated in the context of textile wettability using a canonical model consisting of arrays of parallel cylinders, and has since been extensively applied in the design of a diverse range of non-wetting textured surfaces including fabrics.[26,27] Michielsen and Lee[20] recognized the hierarchical nature of

multifilament woven fabrics and recursively extended the Cassie-Baxter model to predict the apparent contact angle of a water drop on a superhydrophobic multifilament woven fabric. In their analysis, Michielsen and Lee introduce two generations of hierarchy. At the first level of hierarchy (which we denote $n = 1$), they consider the yarn as a series of large parallel cylinders of radius R_1 woven at a 30° angle resulting in a half-spacing of $D_1 = R_1(\sqrt{3} - 1)$. The value of the apparent contact angle of the liquid drop on the yarn is then determined by a second level of hierarchy ($n = 2$); wherein the array of monofilament fibers are also modeled as closely spaced parallel cylinders with the mean half-spacing of the fibers D_2 assumed to be equal to the fiber radius R_2 (*i.e.*, $D_2 \approx R_2$). Michielsen and Lee demonstrate that their recursive model can be used to characterize the water-repellency of multifilament woven fabrics.[20] We extend this model to also consider higher levels of texture, which might be generated, for example, by deposition of various structured nanoparticles. The addition of spherical[7,28–30] and cylindrical[31–33] nanoparticles has been shown to improve the non-wetting character of various fiber- and fabric-based materials. The model we propose can be applied to any such multi-level structure, composed of cylindrical or spherical units, and illustrates how an additional level of nanotexture can dramatically enhance the degree of liquid repellency.

In this work, we initially perform a series of contact angle measurements on a set of nine dip-coated oleophobic woven fabrics with varying yarn radius and half-spacing (see Table 1) using probe liquids of decreasing surface tensions (*i.e.*, $\gamma_{lv} = 72.1$ mN/m to 25.3 mN/m). We observe that the trends of macroscopic apparent contact angles and the transition to the fully-wetted Wenzel state are analogous across all nine dip-coated woven fabrics despite the differences in construction. A modified version of the hierarchical model of Michielsen and Lee was fit to the measured contact angle data on each dip-coated fabric allowing for the determination of a single dimensionless geometrical parameter (D_1^*) that describes the observed wetting behavior on each woven fabric. The model further predicts the existence of a critical value of the equilibrium contact angle of

$\theta_E^{(c)} \approx 57^\circ$, below which a liquid drop will spontaneously transition to the fully wetted Wenzel state *via* a wicking mechanism. The introduction of an additional higher order micro/nano-texture on the fibers ($n = 3$) is necessary to overcome this limit. Finally, we provide an experimental example of how introducing a spherical microtexture on the individual fibers can be used to overcome this limit and produce a strongly oleophobic fabric.

Materials and Methods

Characterization of Fabrics

A set of nine multifilament woven fabrics (four polyester and five nylon, International Textile Group) were investigated. Representative Scanning Electron Micrograph (SEM) images of each of the nine fabrics are provided in the Supporting Information. An image analysis program (ImageJ, NIH)[34] was used to measure the mean radius and half-spacing of the fiber bundles in both the warp and weft directions. The four polyester-based fabrics are labeled A to D and the remaining Nylon-based fabrics are labeled E to I. In Table 1, we provide a summary of the fabric type, measured values of mean diameter of the yarn in the orthogonal warp ($2R_{\text{warp}}$) and weft ($2R_{\text{weft}}$) directions (warp and weft directions were defined arbitrarily), the mean spacing between warp yarns ($2D_{\text{warp}}$) and weft yarns ($2D_{\text{weft}}$).

Substrate coating

In order to confer liquid-repellent behavior to the woven fabrics, a dip-coating technique[4] was used to deposit a low surface-energy coating to the fabrics. A 50/50 wt% solution of fluorodecyl polyhedral oligomeric silsesquioxane (fluorodecyl POSS; $\gamma_{sv} \approx 10$ mN/m)/Tecnoflon (BR9151; Solvay Solexis; $\gamma_{sv} \approx 12$ mN/m) with a total solids concen-

Table 1: The base material used for fabric construction, values of the yarn half spacing in the warp ($D_{1,\text{warp}}$) and weft ($D_{1,\text{weft}}$) directions, and the yarn radius in the warp ($R_{1,\text{warp}}$) and weft ($R_{1,\text{weft}}$) directions for the fabrics used in this study. Yarn half-spacing (D) and radius values (R) have an uncertainty of ± 5 μm. Corresponding images are provided in the Supporting Information.

Fabric	Material	Yarn Half-Spacing (μm)		Yarn Radius (μm)	
		$D_{1,\text{warp}}$	$D_{1,\text{weft}}$	$R_{1,\text{warp}}$	$R_{1,\text{weft}}$
A	PET	100	90	140	150
B	PET	180	140	110	100
C	PET	230	110	140	120
D	PET	70	190	90	90
E	Nylon	240	130	140	130
F	Nylon	150	90	180	70
G	Nylon	180	70	100	90
H	Nylon	210	130	170	100
I	Nylon	210	300	210	200

tration of 20 mg/ml was prepared using the HCFC solvent Asahiklin (AK225, Asahi Glass Company). All fabrics were initially dipped in the fluorodecyl POSS/Tecnoflon solution for 2 minutes, and then allowed to dry in ambient atmospheric conditions for 5 minutes. The fluorodecyl POSS/Tecnoflon dip-coating treatment deposits a thin ($\sim$ 200 nm) uniform conformal oloephobic coating[4] onto the individual fibers of the woven fabric, and thus allows us to control the wetting behavior across the various fabrics, without altering the underlying geometrical structure. The Tecnoflon is a fluoroethyene copolymer that acts as an elastomeric binder conferring flexibility and durability to the coating.[35]

To impart random corpuscular microstructures ($D_{mean} \approx 5$ μm) on the fabrics a spray-coating technique previously developed in our laboratory was used.[36] A 50/50 wt% solution of fluorodecyl POSS/Poly(methyl methacrylate) (PMMA; $M_w = 102\ kg\ \text{mol}^{-1}$) with a total solids concentration of 50 mg/ml was dissolved in Asahiklin. This solution was lightly sprayed onto the fabrics from a distance of 20 cm until a layer of spherical microtexture was deposited onto the individual fibers of the fabric.

Contact Angle Measurements

Contact Angle (CA) measurements were carried out using a ramé-hart goniometer after vertically depositing a drop of $V \approx 5\mu$L on each fabric sample. The probe liquids used in this study were reagent grade deionized (DI) water, dimethyl sulfoxide (DMSO), methylene iodide, ethylene glycol, rapeseed oil, dimethyl methylphosphonate (DMMP), hexadecane, decane, tributyl phospate, methanol, 2-propanol, and heptane. The reported contact angle values represent averages over four or more measurements taken at different locations on the sample.

Theoretical Framework

Flat substrates with low surface energies on the order $\gamma_{sv} \sim 10$ mN/m exhibit equilibrium Young's contact angles with water drops ($\gamma_{lv} = 72.1$mN/m) that are larger than 90°.[26,27] However, drops of various oils and low surface tension liquids (*e.g.*, hexadecane; $\gamma_{lv} = 27.5$mN/m) deposited on the same low energy surface result in Young's contact angles that are much smaller (*i.e.*, $\theta_E < 90^\circ$).[35] Therefore, chemically treated flat surfaces with very low surface energies are typically still oleophilic to liquids with surface tensions $\gamma_{lv} \lesssim 30$ mN/m. The introduction of textured, re-entrant surface topographies (*e.g.*, nanonails, hoodoos, or the cylindrical fibers and yarns of woven fabrics) is necessary to enable the low surface tension liquid drop to rest in a metastable non-wetting Cassie-Baxter state.[1,16]

Cassie and Baxter[24] modeled the behavior of liquid drops on monofilament textiles as an array of parallel cylinders supporting a composite solid-liquid-air interface to obtain their well-known equation, which can be expressed in the following form:[16]

$$\cos\theta^* = -1 + \frac{1}{D^*}\left[(\pi - \theta_E)\cos\theta_E + \sin\theta_E\right] \tag{1}$$

Here, θ^* is the macroscopic apparent contact angle exhibited by the liquid drop deposited on the array of cylinders, θ_E is the corresponding Young's contact angle on a flat surface exhibiting an identical surface chemistry to that of the cylinder, and $D^* = (R + D)/R$ is a dimensionless geometric parameter defined in terms of the half-spacing between the cylinders D and the radius of the cylinder R. This simple one-dimensional cylindrical model is widely used to model the wetting of monofilament textiles.

However, Michielsen and Lee[20] draw attention to the hierarchical nature of multifilament woven fabrics, for which equation 1 cannot directly be applied and needs to be recursively modified. We illustrate the hierarchical structure of a typical fabric in Figure 1, where we show a series of Scanning Electron Micrographs (SEMs) on a multifilament woven fabric that demonstrates two levels of hierarchy corresponding to the bundled yarn and individual fibers. Figure 1a is an SEM of a woven nylon-based fabric (Fabric G) consisting of a uniform weave structure. The fabric has been dipcoated in a solution of 50 wt% fluorodecyl POSS/Tecnoflon to deposit a conformal low-surface-energy coating. The uniform and regular weave that we observe in Fabric G is contrasted to a more loosely-woven polyester-based fabric (Fabric B) that is marked by the presence of weave openings between the warp and weft directions. The presence of these weave openings is captured by changes to the half spacing and radius of the bundled yarns. Therefore, at a macroscopic or 'coarse-grained' level, we expect the geometry of the bundled yarn to influence the wetting behavior of liquid drops on the woven fabric. In Figures 1c and 1d, we show micrographs at two different magnifications of a cured drop of a silicone elastomer (Sylgard 184, Dow Corning; $\gamma_{lv} \approx 25$ mN/m) that has been deposited vertically on the dip-coated oleophobic Fabric G, and subsequently heat treated for 20 minutes at 80 °C to cure. At this higher level of magnification, the inner hierarchical cylindrical structure of the individual fibers is immediately evident. The fibers are densely packed, with radii that are an order of magnitude smaller than the bundled yarn. In Figure 1d, we show the topographical details of the wetted perimeter of the cured silicone drop on the collection

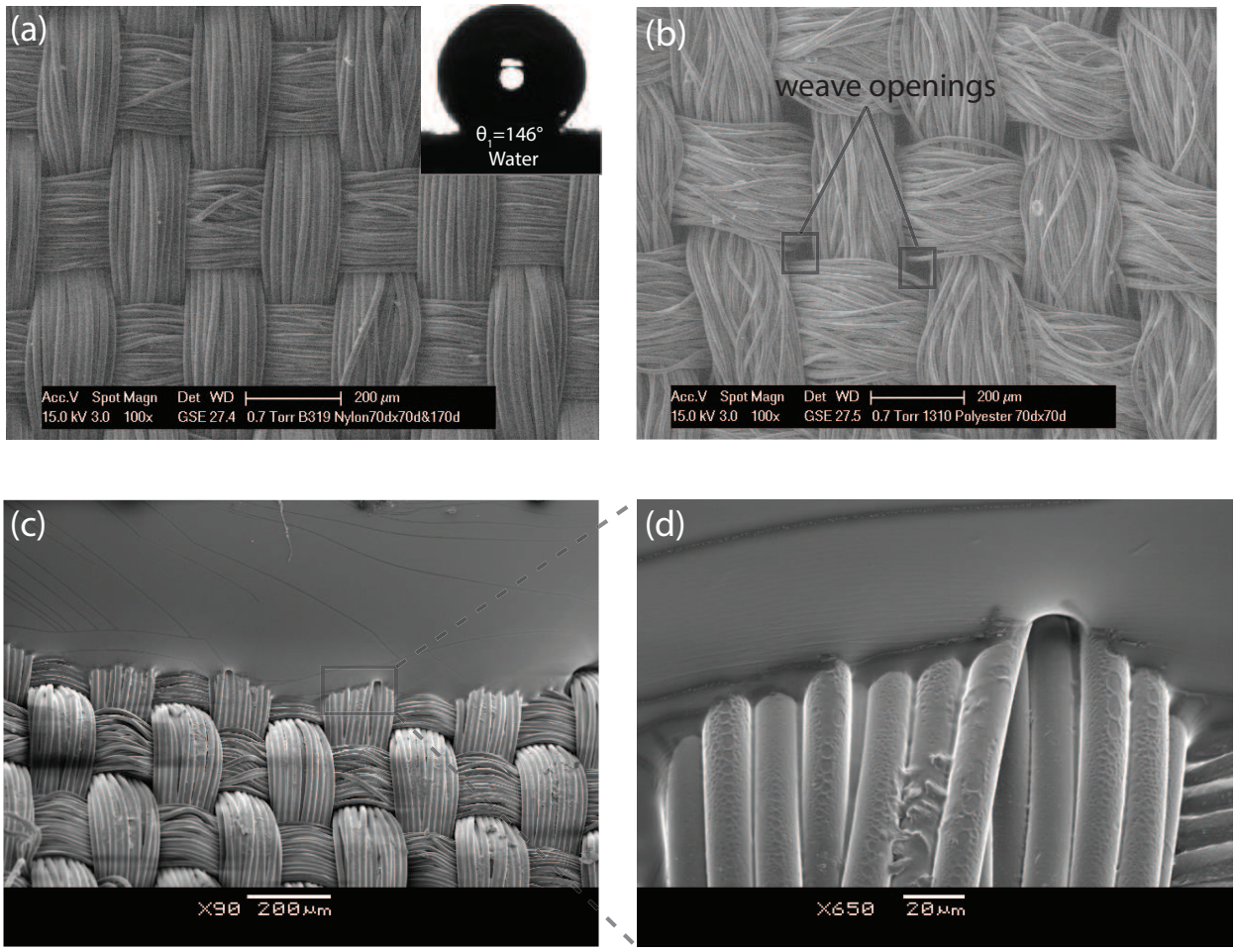

Figure 1: (a) Scanning Electron Micrograph (SEM) of a plain-woven Nylon fabric (Fabric G) which has undergone a hydrophobic treatment by dipcoating in a 50/50 fluorodecyl POSS/Tecnoflon solution. The inset shows a drop of water ($\gamma_{lv} = 72.1$ mN/m) vertically deposited onto the fabric exhibiting a high apparent contact angle of $\theta_1 = 146°$; (b) SEM of a Polyester fabric (Fabric B) exhibiting randomly located weave openings in the woven structure; (c,d) SEM micrographs of the contact line structure of a cured PDMS ($\gamma_{lv} \approx 25$ mN/m) drop resting on Fabric G at different magnifications corresponding to different textural length scales in the fabric. (c) illustrates the shape of the contact line at a length scale corresponding to the bundled yarn of the woven fabric, while (d) captures the tortuosity of the contact line at the scale of the individual fibers within a bundle.

of individual fibers. These small, tightly bundled fibers play a key role in determining the critical surface tension at which a millimetric liquid drop transitions to the Wenzel state and is subsequently imbibed into the fabric.

The self-similar cylindrical structures that are observed in Figure 1(a-d) suggest that Eqn. 1 needs to be recursively applied to the smaller individual fibers and larger bundled yarn to predict the apparent contact angles of liquid drops sitting on multifilament woven fabrics. Here, we apply the recursive framework developed by Herminghaus[22] to expand on the work of Michielsen and Lee.[20] Thus, systematically developing a set of equations that can model both multifilament woven and nanotextured woven fabrics.

Modeling Apparent Contact Angles on Multifilament Woven Fabrics

In Figure 2, we illustrate schematically a liquid drop resting on an oleophobic multifilament fabric. The first level of hierarchy ($n = 1$; *cf.* Figure 2a) captures the woven geometry of the yarn which is modeled as an array of parallel cylinders with a radius R_1, half-spacing D_1 and characterized by the dimensionless geometrical parameter $D_1^* = (R_1 + D_1)/R_1$. The value of D_1^* is related to the weave angle α (between the warp/weft directions and the fabric plane) as $D_1^* = \cot\alpha$. Variations in this geometric parameter D_1^* allows us to account systematically for the wetting effects of various weave constructions and the presence of weave openings on the non-wettability of different fabrics. A small value of D_1^* corresponds to fabrics with a very fine weave, while large values of D_1^* indicate a looser weave with higher incidences of weave openings. At the second level of hierarchy ($n = 2$; Figure 2b), we model the packing of individual fibers into bundles with radius R_2 and mean half-spacing D_2, that are characterized by a dimensionless length scale $D_2^* = (R_2 + D_2)/R_2$. A consequence of constructing the yarn as a collection of tightly bundled fibers is that, for multifilament woven fabrics, the value of the inter-fiber spacing $D_2 \to 0$ (as seen in Figure 1d) which leads to $D_2^* \to 1$. The local effective contact angle of the liquid meniscus that is established on the array of individual fibers is

denoted as θ_2. For the plain weave multifilament fabrics that we have discussed so far, the hierarchy of equations terminates at $n = 2$. The equilibrium contact angle that characterizes the nature of the coating applied to the individual fibers is denoted as θ_E. To define canonically the hierarchical nature of these plain weave fabrics, we denote these two-level cylindrical structures as a CC fabric, as we recursively apply eq 1 twice. Therefore, the set of equations that govern the wetting of a liquid drop on a multifilament woven fabric (or CC fabric) with $n = 2$ is given by eq 2a and 2b:

$$\cos\theta_1 = -1 + \frac{1}{D_1^*}\left[(\pi - \theta_2)\cos\theta_2 + \sin\theta_2\right] \tag{2a}$$

$$\cos\theta_2 = -1 + \left[(\pi - \theta_E)\cos\theta_E + \sin\theta_E\right] \tag{2b}$$

Eq 2a predicts the macroscopic apparent contact angle θ_1 of a droplet placed on the CC fabric while eq 2b governs the apparent contact angle θ_2 of the liquid meniscus on an array of individual fibers that are tightly bundled (with $D_2^* \to 1$). For a wide range of liquids, the mapping implied by eqs 2a and 2b amplifies the local equilibrium contact angle (θ_E) to a new (larger) value of θ_1 on the hierarchically textured surface, thus enhancing the non-wettabilty or "repellency" of the fabric. We will extend this model to a third level of hierarchy as shown schematically in Figure 2(d).

Pressure driven transition from the Cassie-Baxter to Wenzel state on multifilament fabrics

The equilibrium contact angle θ_E can be lowered by (i) depositing liquid drops with lower surface tensions (such as oils) for a given chemical coating on the fibers or (ii) modifying the surface chemistry of the fibers resulting in larger values of surface energy (γ_{sv}) for a given liquid drop. In either scenario, as θ_E decreases, the liquid drop will progressively wet larger fractions of the fabric until it eventually undergoes a transition to the fully

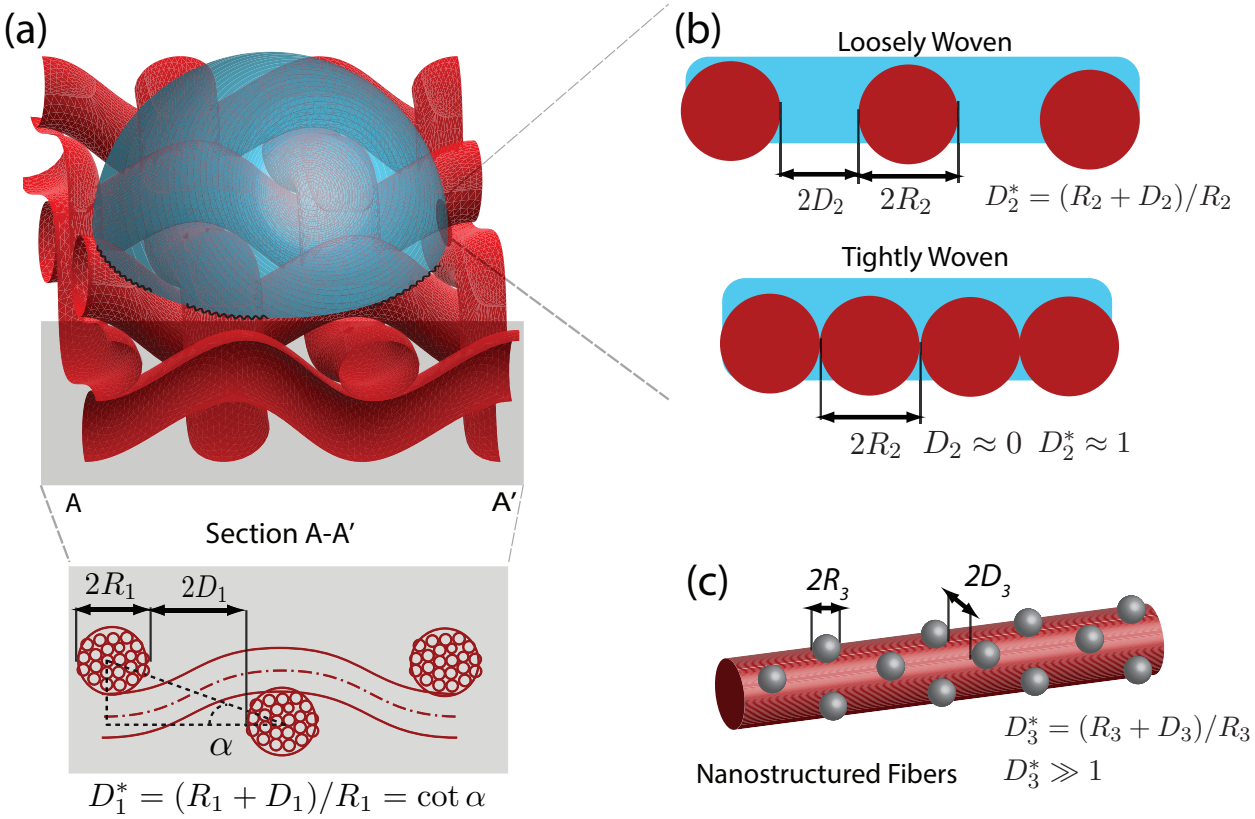

Figure 2: (a) Schematic of an axisymmetric liquid drop on a model sinusoidal non-wetting woven fabric showing different levels of hierarchy. The AA′ plane illustrates the cross-sectional view of the periodic woven structure, consisting of bundled yarns of diameter $2R_1$ separated by a distance $2D_1$. The dimensionless geometric parameter D_1^* is related to the angle of weave α as $D_1^* = (R_1 + D_1)/R_1 = \cot\alpha$; (b) Schematic of the second level of hierarchy depicting the location of the contact line resting on the individual non-wetting fibers which compose the yarn. The fibers are modeled as parallel cylinders of diameter $2R_2$ separated by a distance $2D_2$. The packing of the fibers is governed by the dimensionless geometric parameter $D_2^* = (D_2 + R_2)/R_2$ which is taken to be $D_2^* \approx 1$ (corresponding to the tightly woven limit) consistent with the SEM micrographs shown in Figure 1d; (c) Schematic of a third level of textural hierarchy, with the individual fibers decorated by an array of spherical micro- or nano-particles of radius $2R_3$ and a mean spacing distance of $2D_3$. The packing of the spherical particles is governed by the dimensionless parameter $D_3^* = (R_3 + D_3)/R_3$.

wetted Wenzel state. The Cassie-Baxter to Wenzel transition is driven by the pressure differential that exists across the composite liquid-air interface, and occurs either by a depinning or sagging mechanism.[2,37] This transition occurs as a sequential cascade in hierarchical structures, with the larger air pockets trapped between textural features at the larger length scales ($n = 1$) readily prone to collapse. When liquids with large values of θ_E (*i.e.*, high surface tension liquids) are deposited on multifilament fabrics, they wet only the tops of the woven yarns. This has been demonstrated both by direct visualization and finite element simulations of water on arrays of nonwetting cylinders.[38] However, upon decreasing the value of θ_E, the meniscus descends into the texture until it transitions to resting on the individual fibers that comprise the warp (weft) yarn that lies underneath two adjacent weft (warp) yarns (see Figure 1c). Therefore, the eventual wetting transition to the fully wetted Wenzel state is determined by the smaller length ($n = 2$, fibers) on heirarchical structures such as multifilament woven fabrics. The critical (or breakthrough) pressure difference (ΔP_b) across the liquid-air interface at which the drop irreversibly transitions to the fully-wetted Wenzel state at the largest defect site can be expressed for an array of parallel cylinders as:[37,38]

$$\Delta P_b = (\gamma_{lv}/R_2)\,[\sin(\theta_E - \vartheta_c)/(D_2^* - \sin\vartheta_c)] \tag{3}$$

Where R_2 is the radius of the fiber at the second level of hierarchy and ϑ_c is the critical angular position of the contact line on the cylinder at the onset of transition.[37] At this critical angular position, the transition can occur by either a depinning or a sagging mechanism.

When a liquid drop of surface tension γ_{lv} and radius $r_{\text{drop}} \sim V_{drop}^{1/3}$ is deposited on an array of cylinders, the Laplace pressure inside the drop is $\Delta P_l = 2\gamma_{lv}/r_{\text{drop}}$. A spontaneous transition to the fully-wetted Wenzel state is expected to occur when the Laplace pressure (ΔP_l) exceeds the breakthrough pressure (ΔP_b). The equilibrium contact angle corresponding to the liquid drop at which this critical wetting transition occurs (leading

to a loss of the non-wetting character of the fabric) is denoted as $\theta_E^{(c)}$. A crucial feature of the wetting transition arises from the thermodynamic metastability of the non-wetting Cassie-Baxter state described by eq 1 when $\theta_E < 90^\circ$ (*e.g.*, most oils) and a wetting transition can be nucleated by a single localized defect.[16] The inverse dependence of eq 3 on the feature length scale (R_2) means that the largest defect site in the periodic array acts as the initial nucleation site for the Cassie-Baxter to Wenzel transition. In our calculations below, we assume a defect-free tightly bundled packing of uniform radius fibers with $D_2^* \approx 1$.

In the experiments performed, the drop radius of the probe liquid is fixed as $r_{\text{drop}} \approx$ 1.5 mm. For a liquid drop of heptane ($\gamma_{lv} = 20.1$ mN/m; $\theta_E = 63^\circ$) resting on a planar array of cylinders corresponding to the smallest length scale in the fabric (*i.e.*, $n = 2$; with a fiber spacing ratio of $D_2^* \approx 1$ and a fiber radius of $R \sim 10$ μm), the expected ratio of the breakthrough pressure to the Laplace pressure is $\Delta P_b / \Delta P_l \approx 36$, which suggests that the drop is expected to be stable. However, the tight packing of the bundled fibers provides an alternate route to the Wenzel transition by a wicking mechanism. When the apparent contact angle $\theta_2 \to 0$ on the individual fibers shown in Figure 2b with decreasing values of θ_E, the Cassie-Baxter state supported at the second level of hierarchy (*i.e.*, $n = 2$, between the tightly packed fibers) undergoes a wetting transition and the liquid is imbibed completely into the fiber bundle spreading along the individual fiber filaments. Setting $\cos\theta_2 = 1$ in eq 2b, we solve this implicit equation to obtain a critical value of $\theta_E^{(c)} \approx 57.2^\circ$ when this wetting transition occurs. Physically, this implies that a liquid drop with an equilibrium contact angle *smaller* than this critical value will completely wet the individual fibers and be imbibed into the fabric irrespective of the larger scale geometry of the weave. The loss of the Cassie-Baxter composite state at the $n = 2$ level of hierarchy results in the liquid drop rapidly wicking along the individual fibers until the entire fabric is wetted. Therefore, even if a liquid drop initially exhibits a fairly large macroscopic apparent contact angle on the fabric (*i.e.*, $\theta_1 \gg 90^\circ$), as the equilibrium contact angle θ_E approaches $\theta_E^c \approx 57.2^\circ$, it will sharply transition to $\theta_1 = 0$ as the liquid is imbibed into the texture.[39]

Results and Discussion

Characterization of dip-coated oleophobic fabrics using goniometric measurements

Apparent contact angle measurements were performed on each of the nine dip-coated fabrics using probe liquids with sequentially decreasing values of surface tension from water ($\gamma_{lv} = 72.1$ mN/m) to n-heptane ($\gamma_{lv} = 20.1$ mN/m). In Table 2, we report the measured values of the macroscopic static contact angles (θ_1) on the various dip-coated fabrics. We also list the corresponding values of the equilibrium contact angle (θ_E) measured on flat substrates spin-coated with the same fluorodecyl POSS/Tecnoflon solution. While the equilibrium contact angle on flat surfaces can be measured fairly accurately *via* goniometry ($\Delta\theta_E = \pm 1^\circ$), difficulties in precisely establishing the position of the three-phase contact line on the textured fabrics results in larger uncertainties in the measurement of apparent contact angles ($\Delta\theta_1 = \pm 5^\circ$).

All dip-coated fabrics are strongly water repellent exhibiting large macroscopic contact angles of $\theta_1 \approx 135^\circ$ with water drops and are also resistant to wetting by low surface tension hexadecane drops ($\gamma_{lv} = 27.5$ mN/m; $\theta_1 \approx 95^\circ$), emphasizing the oleophobic non-wetting character that the dip-coating process confers on the nylon and PET based materials. As mentioned earlier, the dip-coating process that conformally deposits the fluorodecyl POSS/Tecnoflon coating ensures that the value of θ_E corresponding to a particular probe liquid is systematically controlled. Therefore, the values of θ_E are identical across all fabrics and any variation in the experimentally measured macroscopic contact angle θ_1 is attributable to the geometry of the outer weave, and in particular to the value of D_1^* (related to the yarn weave angle α as $D_1^* = \cot\alpha$). In each of the fabrics, the macroscopic apparent contact angle decreases with lower surface tension liquid drops (*i.e.*, correspondingly smaller values of θ_E), indicative of progressively larger solid/liquid wetted fractions as more of each individual cylindrical fiber is wetted until eventually a wetting

Table 2: Summary of the surface tension (γ_{lv}), equilibrium contact angle on a flat fluorodecyl POSS/Tecnoflon coating (θ_E), and apparent contact angles (θ_1) on the nine PET and Nylon fabrics fabrics for the thirteen probe liquids of interest. († - Dimethyl methylphosphonate)

Probe Liquid	γ_{lv} (mN/m)	$\theta_E(\pm1^\circ)$	Dip-coated Fabrics $\theta_1(\pm5^\circ)$								
			A	B	C	D	E	F	G	H	I
Water	72.1	109	130	129	140	142	133	133	132	135	123
Dimethyl sulfoxide	43.5	97	114	116	121	115	121	106	109	113	107
Methylene Iodide	50.8	96	103	105	107	104	116	108	105	115	101
Ethylene Glycol	47.7	96	114	113	127	131	132	116	113	103	98
Rapeseed Oil	35.5	92	111	118	125	111	124	110	108	122	107
DMMP†	36.7	88	89	94	110	80	91	95	102	93	101
Hexadecane	27.5	83	0	95	97	91	111	97	92	90	86
Dodecane	25.4	79	0	92	96	88	97	83	84	81	79
Decane	23.8	79	0	84	92	76	-	79	83	80	72
Tributyl Phosphate	27.8	71	0	84	77	85	64	0	77	-	84
Methanol	22.1	66	0	84	85	72	82	0	76	84	69
2-Propanol	23.3	65	0	81	0	0	0	0	0	0	0
Heptane	20.1	63	0	0	0	0	0	0	0	0	0

transition occurs to the Wenzel state. We perform a non-linear regression of the measured values of θ_1 and θ_E using eq 2a and 2b to obtain a best-fit estimate of the dimensionless textural parameter D_1^* that describes the spacing between the yarns for each fabric.

The results of these regression fits are depicted graphically in Figures 3(a-d). The cosines of the experimentally measured values of the macroscopic apparent contact angle ($\cos\theta_1$) are plotted against the cosines of the equilibrium contact angles ($\cos\theta_E$) for four representative dip-coated nylon (Fabrics G and I) and polyester (Fabrics B and C) fabrics with differing weaves. We can use the recursive model described by eq 2a and 2b to obtain two predicted non-wetting curves (corresponding to the warp and weft directions) using values of R_1 and D_1 that are obtained from microscopy (see Table 1). These curves are plotted as solid blue lines in Figures 3(a-d), and represent the upper and lower bounds to the microscopy-based model predictions of θ_1 (bounding the region shaded in blue). In Table 3, the values of the best-fit textural parameter for all nine fabrics are listed, along

with the microscopy based estimates along the warp/weft directions.

Table 3: Fitted values of D^* and corresponding values determined from microscopy for the nine PET and nylon fabrics of interest.

Fabric	D_1^* from Fitting	D_1^* from Microscopy	
		$D_{1,\text{warp}}^*$	$D_{1,\text{weft}}^*$
A	1.2 ± 0.2	1.6	1.8
B	1.7 ± 0.3	2.4	2.6
C	1.8 ± 0.2	1.9	2.7
D	1.5 ± 0.3	1.7	3.1
E	1.7 ± 0.3	2.0	2.6
F	1.3 ± 0.1	1.8	2.4
G	1.5 ± 0.2	1.9	2.8
H	1.5 ± 0.3	2.2	2.3
I	1.4 ± 0.2	2.0	2.5

As is evident from Figures 3(a-d) and Table 3, while the best-fit estimates of D_1^* using the simple hierarchical model of adjacent parallel cylinders qualitatively captures the trends in the non-wetting behavior of the various fabrics, these values are systematically smaller than values that are obtained from microscopy along the warp and weft directions. This result is expected and stems from the fabric possessing three-dimensional structures that protrude into the liquid increasing the real solid fraction of the interface and decreasing the effective D_1^*. A more accurate model would require detailed calculation of the topography of the wetted patches that form on the true woven structure using a program such as Surface Evolver.[40] However, despite the significant simplification involved in our 1D cylindrical array model, some important insights underlying the non-wetting behavior of the fabrics can be obtained by application of the hierarchical model. First, despite the differences in fabric construction the values of $D_{1,\text{warp}}^*$ and $D_{1,\text{weft}}^*$ all lie between $1.6 \leq D^* \leq 3.1$. Our best fit values of D_1^* are similar for all fabrics (between 1.2 and 1.8), and this uniformity is expected due to the very similar nature of the weave angles in all plain weave fabrics, where the geometry of the tight weave offers little flexibility in choosing values of D_1^*. For example, Michielsen and Lee[20] estimate a

weave angle of $\alpha \approx 30^\circ$ (corresponding to a value of $D_1^* \approx 1.7$). This intrinsic constraint on the magnitude of apparent contact angles that can be attained on a plain weave fabric requires the introduction of an additional micro- or nanotextured length scale to further enhance the nonwetting character of fabrics.

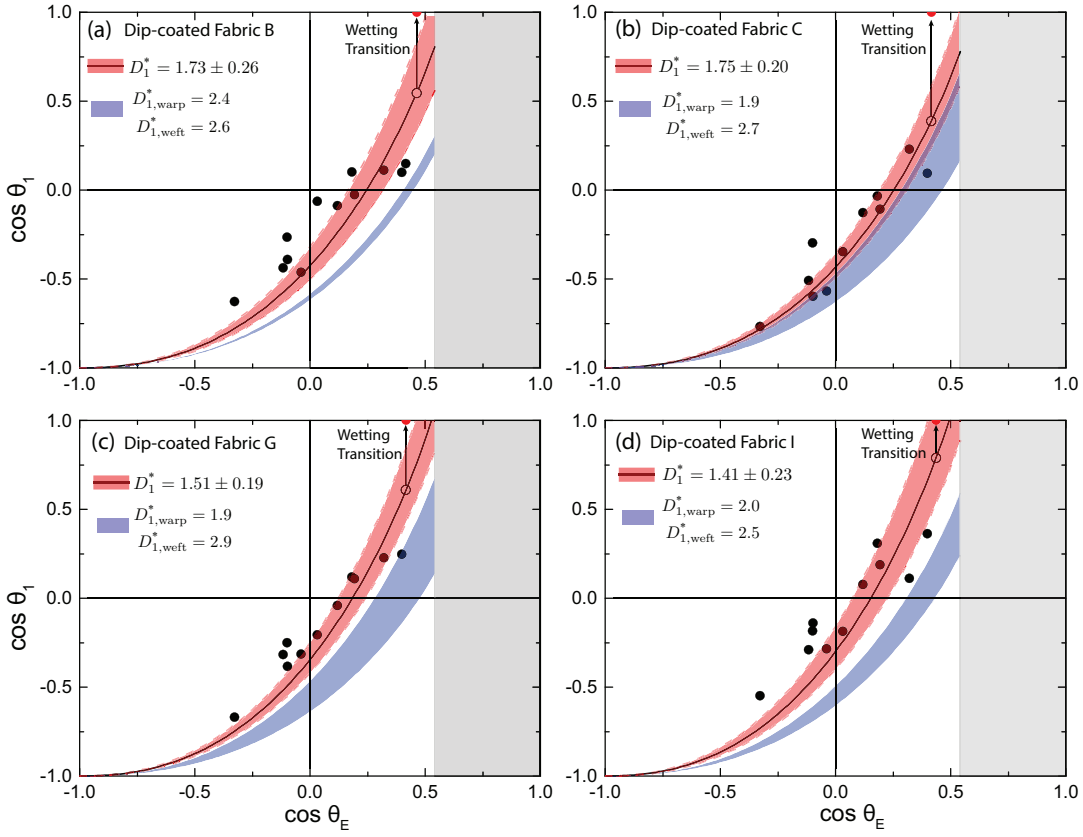

Figure 3: Plot of the cosine of the apparent contact angle $\cos\theta_1$ against the equilibrium contact angle $\cos\theta_E$ on four dip coated fabrics (a) Fabric B (b) Fabric C (c) Fabric G (d) Fabric I. The solid black lines depict the best fit of D_1^* to eq 2 for each of the fabrics (Fabric B: $D_1^* = 1.73 \pm 0.26$; Fabric C: $D_1^* = 1.75 \pm 0.20$; Fabric G: $D_1^* = 1.51 \pm 0.19$; Fabric I: $D_1^* = 1.41 \pm 0.23$) with the 95% confidence interval band shaded in red. We also plot the cosine of the apparent contact angles predicted by the D^* values measured by microscopy (blue shaded region). The upper blue line results from the measured D^* value in the warp direction and the lower blue line results from the value measured in the weft direction. The analogous figures for the remaining five fabrics are shown in the Supporting Information.

Figure 3 and Table 2 also show clearly that for a probe liquid with sufficiently low surface tension, there is a sudden and spontaneous transition to the fully-wetted super-

oleophilic Wenzel state; the liquid drop readily wicks and spreads along the fabric, resulting in a 0° macroscopic contact angle, indicated by the vertical arrow in Figures 3(a-d). For the set of fabrics C-E and G-I, this wetting transition occurs upon contact with propanol ($\gamma_{lv} = 23.3$ mN/m; $\theta_E = 65^\circ$), while fabric B wets with n-heptane ($\gamma_{lv} = 20.1$ mN/m; $\theta_E = 63^\circ$).

In each of the fabrics, we also observe that the critical contact angle $\theta_E^{(c)}$ at which a wicking failure occurs is above the predicted limit of $\theta_E^{(c)} = 57.2^\circ$, consistent with the hierarchical CC model of the woven fabric. The variation of the macroscopic contact angle with a variety of liquids on woven fabrics is captured by the single parameter D_1^* in the CC model. However, the tight bundling of the individual fibers from which the yarn is constructed (*i.e.*, $D_2^* \approx 1$) imposes a lower limit on the surface tension of the contacting liquid that can exhibit oleophobicity.

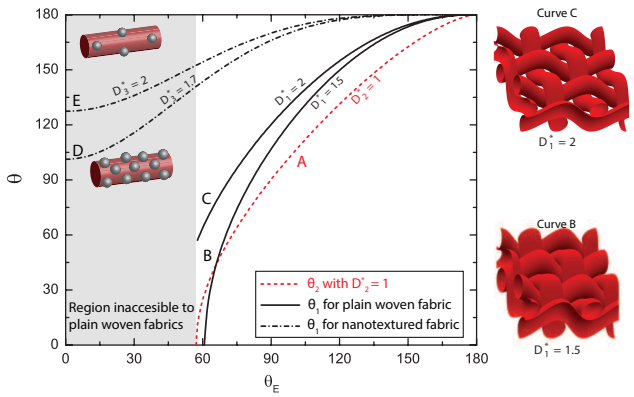

Figure 4: Plot of the contact angles θ_n against the equilibrium contact angle θ_E (predicted by the set of eq 4-5) on a fabric with n levels of hierarchy. The dotted red line A corresponds to the variation of the contact angle on the individual fibers θ_2 with θ_E (predicted by eq 2b) for the tightly woven limit with $D_2^* = 1$. The solid black curves B and C depict the variation of θ_1 for the two values of $D_1^* = 1.5$ and $D_1^* = 2$, respectively, on the plain-woven fabrics with $n = 2$. The model sinusoidal woven geometries corresponding to curves B and C are shown alongside the plot. The shaded region signifies when the individual fibers are fully wetted ($\theta_E \lesssim 57^\circ$) and is inaccessible to the plain weave fabric with two levels of hierarchy $n = 2$. The dashed black lines show the variation of θ_1 with θ_E on woven fabrics consisting of textured fibers with $n = 3$ for two nanoparticle spacings $D_3^* = 1.7$ (Curve D) and $D_3^* = 2$ (Curve E).

Adding a third length-scale of texture to woven fabrics

The undesirable wetting transition, in which the liquid spreads along the closely packed monofilaments of the bundled yarns poses a geometric constraint on the liquid-repellency of woven fabrics. We again emphasize that merely modifying the surface energy by applying various low surface energy coatings is not sufficient to prevent this transition; the introduction of a third level of hierarchy by texturing the individual bundled fibers is required to further amplify the macroscopic contact angle given by the recursive equation set (eq 2). This can be achieved, for example, by the introduction of spherical nanoparticles embedded on the fibers. The recursive equations which determine the apparent contact angle θ_n at each stage of the n generations of the hierarchical self-similar structure are given by eq (4) for a canonical cylindrical geometry (C):[4,20]

$$\cos\theta_n = -1 + \frac{1}{D_n^*}\left[(\pi - \theta_{n+1})\cos\theta_{n+1} + \sin\theta_{n+1}\right] \tag{4}$$

And eq (5) for a spherical geometry (S):[2]

$$\cos\theta_n = -1 + \frac{1}{(D_n^*)^2}\left[\frac{\pi}{2\sqrt{3}}(1+\cos\theta_{n+1})^2\right] \tag{5}$$

In each case the effective contact angle θ_n that can be achieved depends on the geometry of the texture at this n^{th} scale, and the effective contact angle θ_{n+1} that is generated by the next, higher order $(n+1)^{th}$ level of texture. In each case the hierarchical equation set is truncated at the finest scale when the surface is locally flat and $\theta_{n+1} \to \theta_E$. In figure 2c, we show one possible realization using spherical nanoparticles to achieve a third generation of hierarchy in the woven fabric, which we denote as a CCS fabric, as we recursively apply eq 4 for $n = 1, 2$ and eq 5 at $n = 3$. The spherical nanoparticles are embedded into, or deposited onto, the individual fibers of the fabric, and are characterized by a radius R_3, half-spacing D_3 and a corresponding dimensionless parameter $D_3^* = (D_3 + R_3)/D_3$ characterizing the typical spacing of the individual spherical nanoparticles. We further

assume that the chemical coating applied to the spherical nanoparticles is characterized by the same equilibrium contact angle θ_E that is used for the fibers and yarns. The recursive equations governing the nanoparticle textured CCS fabric (conceptualized in Figure 2c) can then be written out explicitly as:

$$\cos\theta_1 = -1 + \frac{1}{D_1^*}\left[(\pi - \theta_2)\cos\theta_2 + \sin\theta_2\right] \tag{6a}$$

$$\cos\theta_2 = -1 + \frac{1}{1}\left[(\pi - \theta_3)\cos\theta_3 + \sin\theta_3\right] \tag{6b}$$

$$\cos\theta_3 = -1 + \frac{1}{(D_3^*)^2}\left[\frac{\pi}{2\sqrt{3}}(1+\cos\theta_E)^2\right] \tag{6c}$$

where θ_3 refers to the apparent contact angle on the individual nanotextured fibers and we assume a tightly woven structure so that $D_2^* \to 1$. The introduction of the third level of structure removes the wicking constraint on oleophobicity, and allows for the design and realization of fabrics which can support liquid drops with very low surface tensions in the metastable Cassie-Baxter state. While eq 6c is written for a CCS nanotextured fabric, an analogous set of equations can be written for a CCC fabric, where the third generation of nanotexture consists of hairy cylinders. In Figure 4, the curves D and E show the variation of the macroscopic apparent contact angle θ_1 with the equilibrium contact angle θ_E for a spherically nanotextured woven CCS fabric described by eq (6a)-(6c) with $D_1^* = 2$, $D_2^* = 1$ and two different values of D_3^*. Larger values of D_3^* result in a lower density of spherical nanoparticles, illustrated by the schematic in the inset of Figure 4. The introduction of the nanotextured length scale greatly enhances the apparent contact angle for the CCS fabric that can be achieved when compared to the equivalent CC fabric with the same value of D_1^* (shown in curve C). In addition, the critical equilibrium contact angle at which the wetting transition occurs in the third generation of hierarchy is controlled by the packing of the spheres.

In order to determine the criteria for the pressure driven wetting transition on the array of nanospheres, we adapt the work of Butt *et al.*[2] on vertically sintered spheres. In Figure 5, we show an illustration of the liquid meniscus between an array of spherical nanoparticles. The position of the contact line on the sphere is a function of the angle ϕ between the contact line, the center of the sphere, and the base of the sphere, and is expressed as $y(\phi) = R_3(1 - \cos\phi)$. The value of ϕ, which sets the location of the contact line, is determined by a balance of the capillary force pulling the interface upwards against the pressure difference across the interface and can be determined from the implicit equation:[2,41]

$$\hat{P} = \frac{\sin\phi \sin(\theta_E - \phi)}{\left(a_l D_3^{*2} - \sin^2\phi\right)} \tag{7}$$

where $\hat{P} = P/P_{\text{ref}}$ and $P_{\text{ref}} = 2\gamma_{lv}/R_3$ is a reference pressure scale that depends on the liquid surface tension γ_{lv} and particle size R_3, and a_l is a lattice constant with $a_l = (2\sqrt{3}/\pi)$ for a hexagonally packed array of spheres and $a_l = (4/\pi)$ for a square packing. When there is no external pressure difference (*i.e.*, $\hat{P} = 0$), the liquid meniscus is flat and the contact line wets the spherical nanoparticle at a height determined by $\phi = \theta_E$. As $\hat{P}$ is increased, the value of ϕ (and therefore, the position of the interface y) steadily decreases according to eq 7 until the Cassie-Baxter state undergoes a transition to the Wenzel state. This transition can occur in one of the following two ways: (i) a depinning mechanism when the pressure exceeds the maximum capillary force that can be supported by eq 7 or (ii) a capillary bulge mechanism when the pressure induces sufficient curvature of the liquid meniscus causing it to touch the underlying substrate on which the spheres are embedded.

In Figure 5c, we plot $\hat{P}$ determined from eq 7 as a function of ϕ for different values of the equilibrium contact angle θ_E and the dimensionless spacing parameter D_3^*. In each of the curves, we see that there is a maximum value of $\hat{P} = \hat{P}_{\text{max}}$ at a particular value of $\phi = \phi_d$ (*i.e.*, $d\hat{P}/d\phi|_{\phi=\phi_d} = 0$). For a given value of D_3^* and θ_E, the maximum pressure

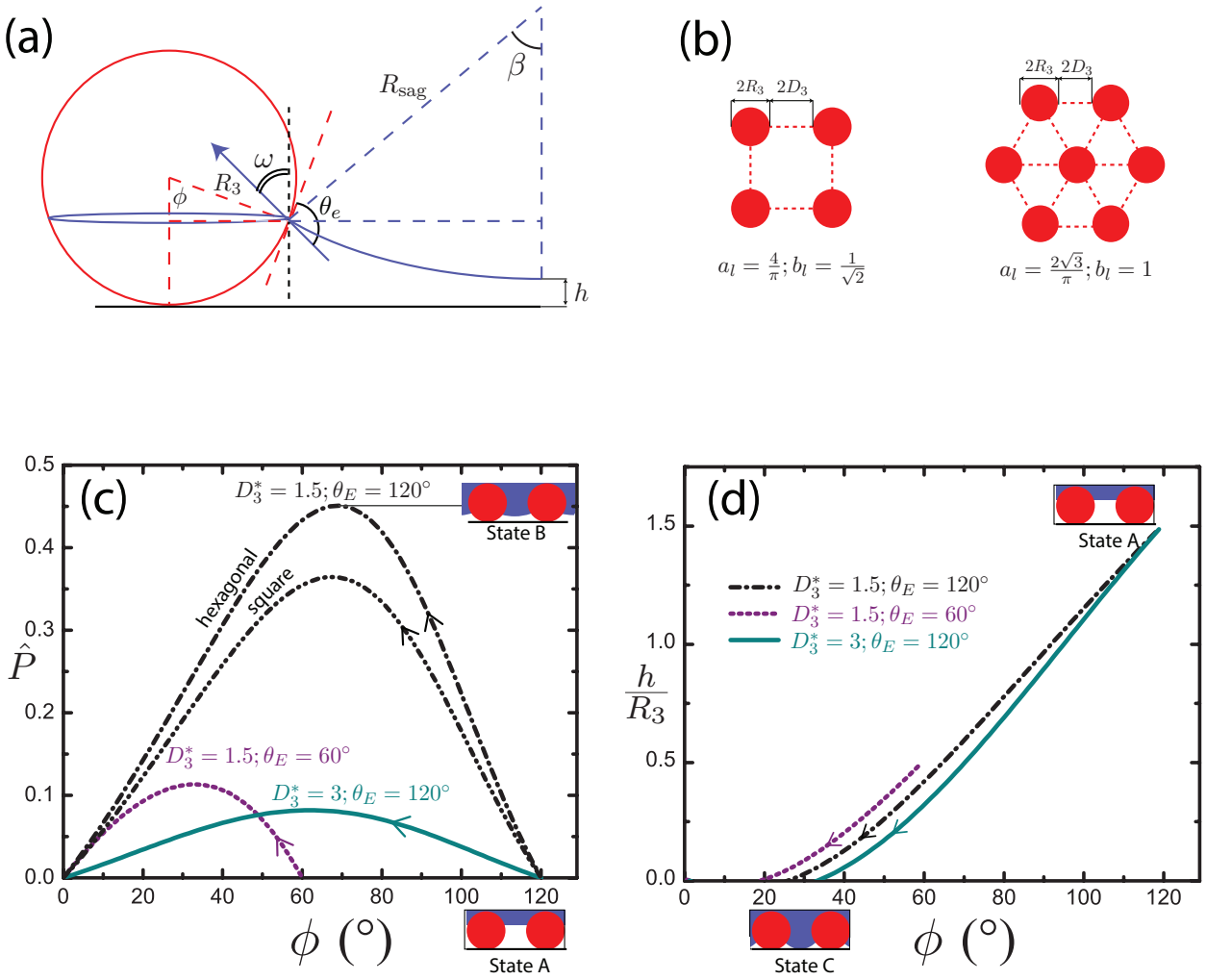

Figure 5: (a) Schematic of the meniscus of a liquid drop resting on a sphere of radius R_3 possessing an equilibrium contact angle θ_E. The contact line subtends an angle of ϕ with the center of the sphere. The pressure differential across the meniscus ΔP drives the formation of the curved meniscus with a radius of curvature R_{sag} that subtends a half-angle β with the vertical. The bottom of the meniscus is at a height h above the bottom surface. (b) Schematic of the top view of an array of spheres arranged in a square and hexagonal lattice. The geometrical lattice parameters a_l, b_l are discussed in the main text. (c) Plot of the dimensionless pressure difference $\hat{P}$ vs the angle ϕ subtended by the contact line to the center of the sphere. Initially, in the absence of any pressure differential ($\hat{P} = 0$), the meniscus is flat and is located at $\phi = \theta_E$ (labeled State A). The value of ϕ decreases with increasing pressure difference $\hat{P}$ until the pressure reaches a maximum at $\phi = \phi_d$ (labeled State B) which corresponds to a depinning transition. (d) Plot of the minimum meniscus height above the bottom substrate h against the subtended angle ϕ showing a gradual decrease until the bottom of the meniscus touches the substrate (*i.e.*, $h = 0$) when $\phi = \phi_s$, signifying a sagging transition (shown in State C). In each of the curves in Fig. 5(c,d), the solid, dashed and dash-dot lines correspond to various values of D_3^* and θ_E as indicated in the figure. Unless otherwise noted, a hexagonal lattice was assumed for the sphere packing.

difference that can be supported is larger for a hexagonal packing of spheres compared to a square array. If the dimensionless pressure difference $\hat{P}$ across the meniscus is larger than the value $\hat{P}_{\max}$, the capillary force acting at the contact line will be unable to balance the pressure force at the interface for any point on the sphere. The composite interface therefore depins and wets when the meniscus physically corresponds to state B depicted in the inset of Figure 6. The depinning transition $\hat{P}_{\text{dep}}$ is therefore the maximum value of $\hat{P}$ at which $d\hat{P}/d\phi = 0$. An expression for the depinning angle ϕ_m is provided by Butt *et al.*. However, while estimating the capillary bulge pressure, Butt *et al.* assume that the location of the contact line is determined by $\phi = \theta_E$, an assumption which is valid only when $\hat{P} \ll 1$. We can derive a more general analytical expression for the height h of the bottom of the curved meniscus (with radius of curvature R_{sag}) above the substrate (as shown in Fig. 5a) as:

$$h = R_3(1 - \cos\phi) - R_{\text{sag}}\,(1 - \cos\beta) \tag{8a}$$

$$\sin\beta = \left(R_3/R_{\text{sag}}\right)\left[b_l(D_3^* - 1) + 1 - \sin\phi\right] \tag{8b}$$

$$\hat{P} = \left(R_3/R_{\text{sag}}\right) \tag{8c}$$

with $b_l = 1$ for a hexagonal lattice and $b_l = 1/\sqrt{2}$ for a square lattice. We show the variation of the height h with ϕ as an external pressure difference is applied in Figure 5d. Initially, when there is no external pressure ($\hat{P} = 0$), the bottom of the meniscus starts at a height $h = R_3(1 - \cos\theta_E)$ above the substrate, depicted by State A in the inset of Figure 5d. As the pressure is gradually increased, the meniscus curvature increases and height decreases. Eventually the meniscus can touch down on the substrate, corresponding to $h = 0$, even if the pressure is still increasing (*i.e.*, $d\hat{P}/d\phi < 0$ in Fig. 5). This corresponds to a sagging transition, and at this point the contact line on the sphere subtends an angle $\phi = \phi_s$. The value of ϕ_s corresponds to the intersection of the curves in Figure 5d with the x-axis, and can be numerically obtained from eq 8a-8c. The value of the dimensionless

pressure difference $\hat{P}_{\text{sag}}$ at which the touchdown of the meniscus first occurs is given by:

$$\hat{P}_{\text{sag}} = \frac{2(1-\cos\phi_s)}{(1-\cos\phi_s)^2 + (b_l(D_3^* - 1) + 1 - \sin\phi_s)^2} \tag{9}$$

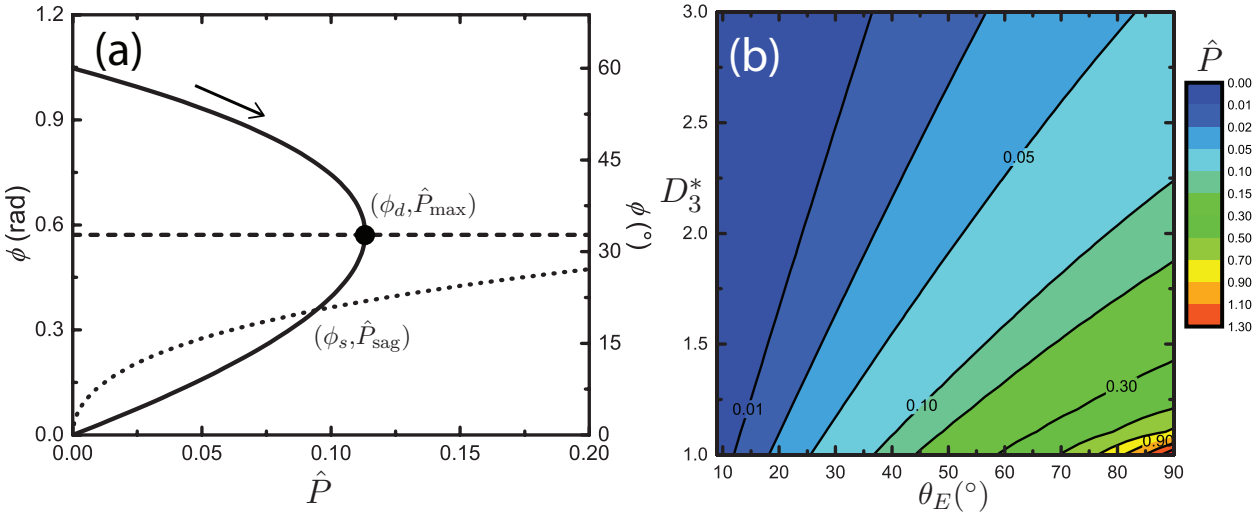

Figure 6: (a) Plot of the location of the contact line characterized by ϕ against dimensionless pressure difference $\hat{P}$ for hexagonally packed spheres with $D_3^* = 1.5$ and $\theta_E = 60^\circ$. The solid curve describes the evolution of the meniscus with pressure via eq 7, where the meniscus initially evolves from $\phi = \theta_E$ when $\hat{P} = 0$. The horizontal dashed line corresponds to the depinning transition limit of $\phi = \phi_d$. The dotted curve plots the variation of the pressure as a function of ϕ corresponding to a sagging transition (eq 9). The intersection of the solid line and the dotted line determines the sagging transition limit of $\phi = \phi_s$; for these paramter values the depinning transition is encountered first (as shown by the solid black circle) (b) Contour plot of the dimensionless breakthrough pressure for various values of the dimensionless geometric spacing D_3^* and equilibrium contact angle θ_E. The breakthrough mechanism corresponds to a depinning transition over the entire range of D_3^* and θ_E shown.

In summary, when there is no external pressure applied, the meniscus initially sits flat at a height h corresponding to $\phi = \theta_E$ (state A in Fig. 5). As the pressure is gradually increased, the meniscus bends and deforms downward and ϕ decreases. The mode of transition from the Cassie-Baxter state to the Wenzel state is determined by the larger of the two angles ϕ_s and ϕ_d (corresponding to the depinning and sagging failure mechanisms, respectively). In Figure 6a, we illustrate this behavior for an array of hexagonally packed spheres characterized by $D_3^* = 1.5$ and $\theta_E = 60^\circ$ as the imposed pressure difference $\hat{P}$ is

increased. The solid line shows the evolution of the location of the meniscus with applied pressure from an initial value of $\phi = \theta_E$ determined by eq 7. The horizontal dashed line indicates the value of ϕ_d at which the depinning transition occurs and the dotted line is a plot of eq 9 as a function of ϕ. The sagging transition, and the value of ϕ_s is found from the intersection of this curve with eq 7. As the value of $\phi_d > \phi_s$, the depinning transition occurs first for this particular configuration. By performing a series of such calculations varying $1 \leq D_3^* \leq 4$ and $0 \leq \theta_E \leq 90^\circ$, we observe that the Cassie-Baxter to Wenzel transition occurs primarily by the depinning transition, even on an single monolayer array of spheres. Our calculations show that as the contact line descends along the surface of the wetted spheres, the smaller wetted perimeter is unable to support the additional pressure force on the curved liquid-vapor surface area and leads to a depinning transition before the lowest point of the meniscus touches the underlying substrate ($h = 0$ or state C in Fig. 5d). This observation of the depinning behavior on an array of spheres is also consistent with the result of Butt *et al.*, who show that the depinning transition is the dominant mode on higher aspect ratio structures, such as an array of two vertically sintered spheres. In Figure 6b, we show contour plots of the dimensionless pressure $\hat{P}_d(\theta_E, D_3^*)$ at which depinning occurs. For a fixed surface coating (which fixes the value of θ_E), the value of the depinning pressure $\hat{P}_d$ steadily decreases as the dimensionless spacing ratio increases. Following the procedure of Butt *et al.*, we can obtain an analytical estimate of the breakthrough pressure in the limit of large $D_3^* \gg 1$. Eq 7 simplifies to the expression, $\hat{P} \cong \sin\phi \sin(\theta_E - \phi)/(a_l D_3^{*2})$ and we can obtain an expression for the dimensional depinning pressure in this limit as:

$$P_d = \left(\frac{2\gamma_{lv}}{R}\right)\left(\frac{1}{a_l D_3^{*2}}\right)\sin^2(\theta_E/2) \tag{10}$$

The pressure at which the depinning transition occurs scales directly with the liquid surface tension ($P_d \propto \gamma_{lv}$), and inversely with the radius of the spherical microstructures ($P_d \propto 1/R$) and with the square of the dimensionless spacing ratio ($P_d \propto 1/D_3^{*2}$).

This implies that small, densely-packed spherical particles decorating individual fibers are needed to construct robustly superoleophobic fabrics. The Laplace pressure inside a liquid drop of radius $r_{drop} \sim (V_{drop})^{1/3}$ deposited on the spherically nanotextured fabric is $P = 2\gamma/r_{drop}$. Equating this pressure with the depinning pressure from eq 10, we can obtain an estimate of the maximum radius of the sphere R that can sustain a low surface tension liquid drop in the Cassie-Baxter state as $R \lesssim (r/a_l)(1/D_3^{*2}) \sin^2(\theta_E/2)$.

Spray-coating of third-length scale on woven fabrics

In order to test the prediction that a third level of structure with a sufficiently small length scale can widen the range of oleophobicity for a selected fabric, we use a spray technique to deposit corpuscular beads onto a dip-coated woven fabric (Fabric E) from a 50/50 wt% poly(methyl methacrylate)/fluorodecyl POSS solution.[36] The spherical beads are formed during the capillary-driven atomization of the non-Newtonian polymer solution by a judicious choice of the solution concentration and molecular weight of the polymer.[36] In Figure 7(a,b) we show SEM images of a spray-coated Nylon fabric (Fabric E) at two different magnifications. The spherical beads are randomly deposited on the fibers with a broad distribution in both the radius ($5\mu\text{m} \lesssim R_3 \lesssim 15\mu\text{m}$) and mean dimensionless spacing D_3^*.

The spray-coated textured fabric exhibits an enhanced liquid-repellent behavior. In Fig. 7c, we plot the cosine of the macroscopic contact angle $\cos\theta_1$ against the cosine of the equilibrium contact angle $\cos\theta_E$ (analogous to Figure 3) for two samples Fabric E that have either been dip-coated to increase the equilibrium contact angle on the fibers $\theta_2 \rightarrow \theta_E$ (black circles) or spray-coated to yield a third level of structure $\theta_3 \rightarrow \theta_E$ (red circles). The effect of introducing the third length scale is apparent in the larger values of the macroscopic contact angle on the sprayed-coated fabric for the various low surface tension liquids when compared to the dip-coated woven fabric. The differences in the roll-off angles between the spray-coated and dip-coated fabrics are shown in Figure

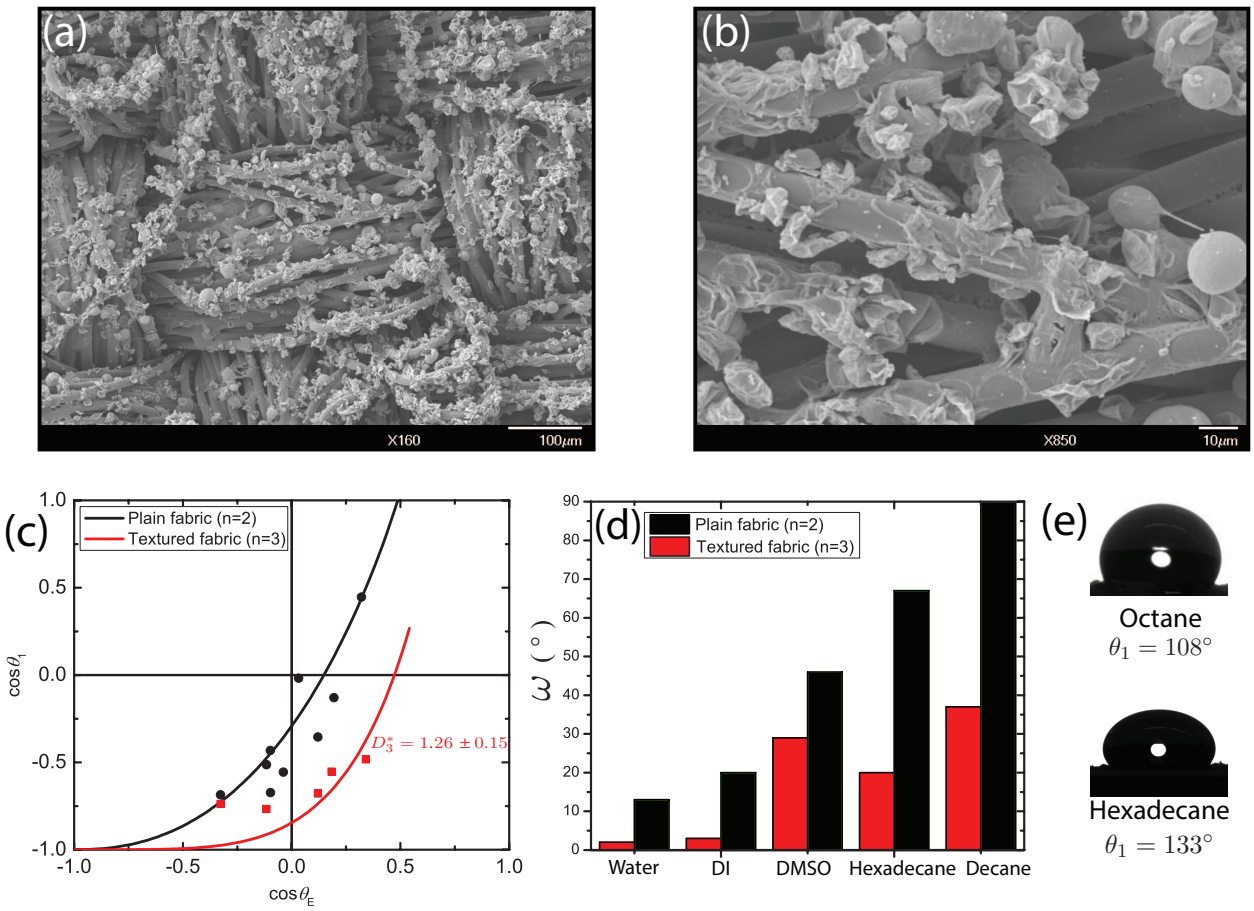

Figure 7: (a) Scanning Electron Micrograph (SEM) of a dip-coated nylon fabric (Fabric E) spray-coated with a 50/50 PMMA/fluorodecyl POSS solution to introduce a spherical microtexture on individual fibers; (b) Magnified SEM showing the spherical PMMA/fluorodecyl POSS microtexture; (c) Plot of the effective contact angle ($\cos\theta_1$) against $\cos\theta_E$ for the dip-coated plain weave fabric (black line) $D_1^* = 1.7 \pm 0.29$ and the spray-coated fabric with $D_3^* = 1.26 \pm 0.15$ (red line); (d) A plot of the roll-off angle ω (in degrees) on the dip-coated plain-woven fabric (black) and spray-coated textured fabric (red) for a range of different liquids; (e) Liquid drops ($V \approx 10$ μL) of hexadecane ($\gamma_{lv} = 27.8$ mN/m) and octane ($\gamma_{lv} = 21.6$ mN/m) vertically deposited on the sprayed fabric shown in (a,b) exhibiting contact angles of $\theta_1 = 133°$ and $\theta_1 = 108°$ respectively.

7d. The textured spray-coated fabrics consistently show smaller roll-off angles for the range of liquids used, indicating a superior oleophobic character. In Figure 7e, we show liquid drops of octane and hexadecane that are deposited onto the spray-coated fabric resulting in macroscopic contact angles of $\theta_1 = 108^\circ$ and $\theta_1 = 133^\circ$, respectively. By contrast, the same sized drop of octane ($V \approx 10\mu$L) completely wets the dip-coated fabric E. The dimensionless spacing ratio of the weave was calculated previously (*cf.* Table 3) as $D_1^* = 1.57 \pm 0.27$ and is shown as the solid black line in Figure 7c. Using this value of D_1^*, which characterizes the geometry of the weave, we can perform a regression of the contact angle data on the spray coated fabric using eq 6a, 6b and 6c to obtain an estimate of the mean spacing ratio of the spherical beads as $D_3^* = 1.49 \pm 0.23$. We also observe that the transition to the Wenzel state on the spray-coated fabric occurs for n-heptane ($\gamma_{lv} = 20.1$ mN/m; $\theta_E = 62^\circ$). This best-fit estimate of D_3^* approximates the corrugated and polydisperse corpuscular beads with varied radii and interparticle spacing (as seen in Figure 7) as a model system of uniformly-spaced, hexagonally-packed array of spheres. By applying the simple model presented in the previous section using this value of $D_3^* \approx 1.5$, we obtain an estimate of the maximum feature size that should be able to support a 1 mm liquid drop of n-heptane as $R_{\min} \approx 100\mu$m, which is an order of magnitude larger than the $5 - 15$ μm structures observed in Figure 7b. However, the origin of this discrepancy can be attributed to the broad distribution of the interparticle spacing in the real spray-coated fabric, and the metastability of the non-wetting Cassie-Baxter state. Local regions of the spray-coated fibers containing a low density of corpuscular spheres and large interbead spacing, act as nucleation sites for the Cassie-Baxter to Wenzel transition. Indeed, by using a value of $R = 10$ μm for the corpuscular structures (consistent with SEM images), we see that the 1 mm drop of n-heptane will locally wet regions where the value of $D_3^* \gtrsim 4.7$ (*i.e.*, $D_3 = R(D_3^* - 1) \approx 37$ μm). An example of potential nucleation sites with large interbead spacing can be seen in Figure 7b. Therefore, it is critical to develop processing techniques which can deposit a uniform and conformal layer of densely packed spherical

structures with minimal defect sizes. This will help prevent wetting transitions on oleophobic fabric surfaces, and allow for even lower surface tension liquids to be supported in the non-wetting state. Our simple spray-coating method clearly demonstrates the benefits of introducing a third re-entrant length scale when designing oleophobic fabrics, as revealed by the ability of the three-scale texture of Fabric E (shown in Fig. 7) to resist wetting by octane.

Conclusions

In this work, we initially performed a series of contact angle measurements on a set of nine dip-coated omniphobic[16] woven fabrics with varying yarn radius (R_1) and half-spacing (D_2^*) using probe liquids of decreasing surface tensions (from water, $\gamma_{lv} = 72.1$ mN/m, to heptane, $\gamma_{lv} = 20.1$ mN/m). The trends of macroscopic apparent contact angles and the transition to the fully-wetted Wenzel state are similar across all nine dip-coated woven fabrics despite the differences in weave construction. Fitting a modified version of the hierarchical two-level model outlined by Michielsen and Lee (2007) to the measured contact angle data allows us to obtain a single dimensionless geometrical parameter (D_1^*) that characterizes the observed wetting behavior on each woven fabric. This dimensionless parameter is related to the weave angle of the fabric, and can rationalize the experimentally measured trends in the apparent contact angles as well as the onset of a spontaneous wetting transition to the fully-wetted Wenzel state. For the particular case of tightly bundled fibers in the fabric yarns, our model further predicts the existence of a critical value of the equilibrium contact angle of $\theta_E^{(c)} \approx 57^\circ$, below which a liquid drop will spontaneously transition to the fully wetted Wenzel state by a wicking mechanism. This is consistent with the observed transition data. We have demonstrated that the introduction of an additional micro/nano-textured length scale on the fibers ($n = 3$) is necessary to overcome this limit and we have developed a three level hierarchical model to

rationalize this effect. We have extended previously developed ideas on pressure-driven Cassie-Baxter to Wenzel transitions in order to provide a framework that guides the selection of particle size, feature density and surface coating at all three length scales. Finally, we provide an example of how introducing a spherical microtexture on the individual fibers using a spray-on technique can be used to extend the range of liquid repellency for a given fabric. The hierarchical equation set given by eq 6, in conjunction with the analysis of stability against meniscus depinning and sagging (eq 7-10), can be used to understand how to maximize the oleophobic character of a woven fabric system.

Acknowledgement

We gratefully acknowledge financial support from the Army Research Office through Contract W911NF-13-D-0001. We thank the Institute for Soldier Nanotechnologies (ISN) and the Center for Material Science and Engineering (CMSE) at MIT for the use of various analytic equipment.

Supporting Information Available

Scanning Electron Micrograph (SEM) images of each of the nine fabrics discussed in the text and wetting plots analogous to those shown in Fig. 3 for Fabrics A, D, E, F, and H. This material is available free of charge via the Internet at `http://pubs.acs.org/`.

References

(1) Tuteja, A.; Choi, W.; Ma, M.; Mabry, J. M.; Mazzella, S. A.; Rutledge, G. C.; McKinley, G. H.; Cohen, R. E. Designing Superoleophobic Surfaces. *Science* **2007**, *318*, 1618–1622.

(2) Butt, H.-J.; Semprebon, C.; Papadopoulos, P.; Vollmer, D.; Brinkmann, M.; Ciccotti, M. Design principles for superamphiphobic surfaces. *Soft Matter* **2013**, *9*, 418–428.

(3) Marmur, A. Superhydrophobic and superhygrophobic surfaces: From understanding non-wettability to design considerations. *Soft Matter* **2013**, *9*, 7900–7904.

(4) Choi, W.; Tuteja, A.; Chhatre, S.; Mabry, J. M.; Cohen, R. E.; McKinley, G. H. Fabrics with Tunable Oleophobicity. *Advanced Materials* **2009**, *21*, 2190–2195.

(5) Kota, A. K.; Kwon, G.; Choi, W.; Mabry, J. M.; Tuteja, A. Hygro-responsive membranes for effective oil-water separation. *Nature Communications* **2012**, *3*, 1025.

(6) Gao, L.; McCarthy, T. J. Artificial Lotus Leaf Prepared Using a 1945 Patent and a Commercial Textile. *Langmuir* **2006**, *22*, 5998–6000.

(7) Ma, M.; Mao, Y.; Gupta, M.; Gleason, K. K.; Rutledge, G. C. Superhydrophobic Fabrics Produced by Electrospinning and Chemical Vapor Deposition. *Macromolecules* **2005**, *38*, 9742–9748.

(8) Coclite, A. M.; Shi, Y.; Gleason, K. K. Grafted Crystalline Poly-Perfluoroacrylate Structures for Superhydrophobic and Oleophobic Functional Coatings. *Advanced Materials* **2012**, *24*, 4534–4539.

(9) Zimmermann, J.; Reifler, F. A.; Fortunato, G.; Gerhardt, L.-C.; Seeger, S. A Simple, One-Step Approach to Durable and Robust Superhydrophobic Textiles. *Advanced Functional Materials* **2008**, *18*, 3662–3669.

(10) Vilčnik, A.; Jerman, I.; Šurca Vuk, A.; Koželj, M.; Orel, B.; Tomšič, B.; Simončič, B.; Kovač, J. Structural Properties and Antibacterial Effects of Hydrophobic and Oleophobic Sol-Gel Coatings for Cotton Fabrics. *Langmuir* **2009**, *25*, 5869–5880.

(11) Deng, B.; Cai, R.; Yu, Y.; Jiang, H.; Wang, C.; Li, J.; Li, L.; Yu, M.; Li, J.; Xie, L.; Huang, Q.; Fan, C. Laundering Durability of Superhydrophobic Cotton Fabric. *Advanced Materials* **2010**, *22*, 5473–5477.

(12) Miao, H.; Bao, F.; Cheng, L.; Shi, W. Cotton fabric modification for imparting high water and oil repellency using perfluoroalkyl phosphate acrylate via γ-ray-induced grafting. *Radiation Physics and Chemistry* **2010**, *79*, 786–790.

(13) Hayn, R. A.; Owens, J. R.; Boyer, S. A.; McDonald, R. S.; Lee, H. J. Preparation of highly hydrophobic and oleophobic textile surfaces using microwave-promoted silane coupling. *Journal of Materials Science* **2011**, *46*, 2503–2509.

(14) Zhang, J.; Seeger, S. Superoleophobic Coatings with Ultralow Sliding Angles Based on Silicone Nanofilaments. *Angewandte Chemie International Edition* **2011**, *50*, 6652–6656.

(15) Lee, H.; Owens, J. In *Advances in Modern Woven Fabrics Technology*; Vassiliadis, S., Ed.; InTech, 2011.

(16) Tuteja, A.; Choi, W.; Mabry, J. M.; McKinley, G. H.; Cohen, R. E. Robust omniphobic surfaces. *Proceedings of the National Academy of Sciences* **2008**, *105*, 18200–18205.

(17) Deng, T.; Varanasi, K. K.; Hsu, M.; Bhate, N.; Keimel, C.; Stein, J.; Blohm, M. Nonwetting of impinging droplets on textured surfaces. *Applied Physics Letters* **2009**, *94*, 133109.

(18) Koishi, T.; Yasuoka, K.; Fujikawa, S.; Ebisuzaki, T.; Zeng, X. C. Coexistence and transition between Cassie and Wenzel state on pillared hydrophobic surface. *Proceedings of the National Academy of Sciences* **2009**, *106*, 8435–8440.

(19) Bird, J. C.; Dhiman, R.; Kwon, H.-M.; Varanasi, K. K. Reducing the contact time of a bouncing drop. *Nature* **2013**, *503*, 385–388.

(20) Michielsen, S.; Lee, H. J. Design of a Superhydrophobic Surface Using Woven Structures. *Langmuir* **2007**, *23*, 6004–6010.

(21) Kawabata, S.; Niwa, M.; Kawai, H. 3—The Finite Deformation Theory of Plain Weave Fabrics Part I: The Biaxial-Deformation Theory. *Journal of the Textile Institute* **1973**, *64*, 21–46.

(22) Herminghaus, S. Roughness-induced non-wetting. *Europhysics Letters* **2000**, *52*, 165.

(23) Paxson, A. T.; Varanasi, K. K. Self-similarity of contact line depinning from textured surfaces. *Nature Communications* **2013**, *4*, 1492.

(24) Cassie, A. B. D.; Baxter, S. Wettability of porous surfaces. *Transactions of the Faraday Society* **1944**, *40*, 546–551.

(25) Cassie, A. B. D.; Baxter, S. Large Contact Angles of Plant and Animal Surfaces. *Nature* **1945**, *155*, 21–22.

(26) Quéré, D. Wetting and Roughness. *Annual Review of Materials Research* **2008**, *38*, 71–99.

(27) Marmur, A. Solid-Surface Characterization by Wetting. *Annual Review of Materials Research* **2009**, *39*, 473–489.

(28) Leng, B.; Shao, Z.; de With, G.; Ming, W. Superoleophobic Cotton Textiles. *Langmuir* **2009**, *25*, 2456–2460.

(29) Hoefnagels, H. F.; Wu, D.; de With, G.; Ming, W. Biomimetic Superhydrophobic and Highly Oleophobic Cotton Textiles. *Langmuir* **2007**, *23*, 13158–13163.

(30) Ramaratnam, K.; Iyer, S. K.; Kinnan, M. K.; Chumanov, G.; Brown, P. J.; Luzinov, I. Ultrahydrophobic Textiles Using Nanoparticles: Lotus Approach. *Journal of Engineered Fibers and Fabrics* **2008**, *3*, 1–14.

(31) Makowski, T.; Kowalczyk, D.; Fortuniak, W.; Jeziorska, D.; Brzezinski, S.; Tracz, A. Superhydrophobic properties of cotton woven fabrics with conducting 3D networks of multiwall carbon nanotubes, MWCNTs. *Cellulose* **2014**, *21*, 4659–4670.

(32) Shirgholami, M. A.; Khalil-Abad, M. S.; Khajavi, R.; Yazdanshenas, M. E. Fabrication of superhydrophobic polymethylsilsesquioxane nanostructures on cotton textiles by a solutionimmersion process. *Journal of Colloid and Interface Science* **2011**, *359*, 530–535.

(33) Liu, Y.; Tang, J.; Wang, R.; Lu, H.; Li, L.; Kong, Y.; Qi, K.; Xin, J. H. Artificial lotus leaf structures from assembling carbon nanotubes and their applications in hydrophobic textiles. *Journal of Materials Chemistry* **2007**, *17*, 1071–1078.

(34) Schneider, C. A.; Rasband, W. S.; Eliceiri, K. W. NIH Image to ImageJ: 25 years of image analysis. *Nature Methods* **2012**, *9*, 671–675.

(35) Meuler, A. J.; Chhatre, S. S.; Nieves, A. R.; Mabry, J. M.; Cohen, R. E.; McKinley, G. H. Examination of wettability and surface energy in fluorodecyl POSS/polymer blends. *Soft Matter* **2011**, *7*, 10122–10134.

(36) Srinivasan, S.; Chhatre, S. S.; Mabry, J. M.; Cohen, R. E.; McKinley, G. H. Solution spraying of poly(methyl methacrylate) blends to fabricate microtextured, superoleophobic surfaces. *Polymer* **2011**, *52*, 3209–3218.

(37) Bormashenko, E.; Gendelman, O.; Whyman, G. Superhydrophobicity of Lotus Leaves versus Birds Wings: Different Physical Mechanisms Leading to Similar Phenomena. *Langmuir* **2012**, *28*, 14992–14997.

(38) Srinivasan, S.; Chhatre, S. S.; Guardado, J. O.; Park, K.-C.; Parker, A. R.; Rubner, M. F.; McKinley, G. H.; Cohen, R. E. Quantification of feather structure, wettability and resistance to liquid penetration. *Journal of The Royal Society Interface* **2014**, *11*.

(39) Chhatre, S. S.; Choi, W.; Tuteja, A.; Park, K.-C. K.; Mabry, J. M.; McKinley, G. H.; Cohen, R. E. Scale Dependence of Omniphobic Mesh Surfaces. *Langmuir* **2010**, *26*, 4027–4035.

(40) Srinivasan, S.; Choi, W.; Park, K.-C.; Chhatre, S. S.; Cohen, R. E.; McKinley, G. H. Drag reduction for viscous laminar flow on spray-coated non-wetting surfaces. *Soft Matter* **2013**, *9*, 5691–5702.

(41) Yarnold, G. D. The hysteresis of the angle of contact of mercury. *Proceedings of the Physical Society* **1946**, *58*, 120–125.

Graphical TOC Entry